Research Article | Vol. 30, No. 15 / 18 Jul 2022 / Optics Express 27967

Optics EXPRESS

High-resolution, wavefront-sensing, full-field polarimetry of arbitrary beams using phase retrieval

MATTHEW N. JACOBS,[1,*] YUKA ESASHI,[1] NICHOLAS W. JENKINS,[1] NATHAN J. BROOKS,[1] HENRY C. KAPTEYN,[1,2] MARGARET M. MURNANE,[1] AND MICHAEL TANKSALVALA[1]

[1] *STROBE Science and Technology Center and JILA, University of Colorado Boulder, Colorado 80309, USA*
[2] *KMLabs Inc., 4775 Walnut St. Building 102, Boulder, Colorado 80301, USA*
[*] *Matthew.N.Jacobs@colorado.edu*

Abstract: Recent advances in structured illumination are enabling a wide range of applications from imaging to metrology, which can benefit from advanced beam characterization techniques. Solving uniquely for the spatial distribution of polarization in a beam typically involves the use of two or more polarization optics, such as a polarizer and a waveplate, which is prohibitive for some wavelengths outside of the visible spectrum. We demonstrate a technique that circumvents the use of a waveplate by exploiting extended Gerchberg–Saxton phase retrieval to extract the phase. The technique enables high-resolution, wavefront-sensing, full-field polarimetry capable of solving for both simple and exotic polarization states, and moreover, is extensible to shorter wavelength light.

1. Introduction

The generation of light beams with engineered structure and wavefront is an extremely active research field due to their potential application in a wide range of areas from imaging to communication [1–9]. Recent advances have made it possible to generate structured light at wavelengths spanning from the THz to the extreme ultraviolet (EUV) and soft X-ray (SXR) regions through control of wavefront, polarization, and orbital angular momentum (OAM) [10–15]. The successful generation of structured beams can be challenging because it often relies on high polarization purity and precise optical alignment. Integration of such beams into a wide range of experiments, metrologies and technologies requires quantitative, high-resolution techniques that can characterize structured beams to ensure that the desired shape is achieved.

Determining the vector electric field of arbitrary-shaped beams typically requires a set of well-calibrated optics and/or a complicated setup involving interferometry or lenslet arrays [15–21]. Calibration is critical for each of these approaches and relies on precise alignment of the analyzing optics. Moreover, implementing such schemes in the EUV and SXR regions of the spectrum is limited, due to the lack of high-quality polarizing optics (waveplates in particular) for these wavelengths.

Recently, a collection of computational imaging techniques, known as coherent diffractive imaging (CDI), have made it possible to circumvent the need for high-quality optics. CDI can measure complex fields by collecting redundant intensity data and using a computational algorithm to extract the phase. For instance, high-resolution, quantitative determination of the scalar electric field can be performed using either ptychography [22,23] or an extended Gerchberg–Saxton (eGS) technique [15,24].

We present an extension of eGS, called Polarimetry with extended Gerchberg–Saxton (PeGS), that combines wavefront sensing with polarimetry to retrieve the full-field polarization of a beam,

#461658 https://doi.org/10.1364/OE.461658
Journal © 2022 Received 20 Apr 2022; revised 9 Jun 2022; accepted 12 Jun 2022; published 15 Jul 2022

with high spatial resolution, using only a rotatable polarizer. In addition to simplifying high-resolution polarimetry with visible light, this could pave the way for a host of short-wavelength metrologies, since it is possible to fully control the polarization and shape of coherent short wavelength high harmonic beams by controlling the driving laser field(s).

This paper is structured as follows: in Section 2, we outline the PeGS technique and show that it recovers the full polarization state at each pixel of the light field. In Section 3, we show experimental results of PeGS when applied to various exotic beams of practical use and scientific import—namely dual-spot beams, full Poincaré beams, and vector and vector vortex beams. Finally, in Section 4 we discuss the reconstructions in more detail and show examples of further analysis that can be performed once the full vector fields have been retrieved.

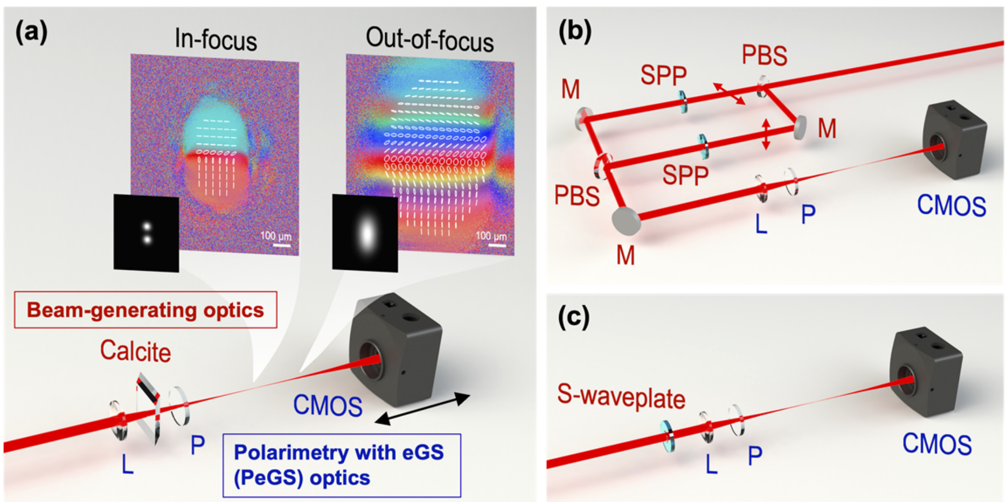

Fig. 1. Experimental setup for characterizing several beams using Polarimetry with extended Gerchberg–Saxton (PeGS). All of the experiments use a Ti:Sapphire oscillator to generate a continuous-wave 785 nm beam, followed by the lens (L) and polarizer (P) and a CMOS camera for collecting intensity measurements of the beam at multiple locations through the focus. The optical components for PeGS are labeled in blue, while the optics used to generate the beams to be characterized are labeled in red. (a) Setup for measuring dual-spot beams. A calcite delay plate is used to prepare the beam in a state that has two orthogonally polarized spots at the focus. Inserts show the total intensity of the beam at the in-focus and out-of-focus planes, as well as the polarization spatial distribution solved by PeGS using the colormap in Fig. 2. (b) Setup for measuring full Poincaré beams (generated by superposing two orthogonally polarized orbital angular momentum beams) using a Mach-Zehnder interferometer to individually alter two collinear beams of orthogonal polarization. Polarizing beam splitters (PBS) and mirrors (M) are used to separate and recombine the orthogonal polarization components, and spiral phase plates (SPP) are used to generate orbital angular momentum beams. (c) Setup for measuring vector and vector vortex beams generated with an S-waveplate.

2. Polarimetry with extended Gerchberg–Saxton (PeGS)

2.1. Background: extended Gerchberg–Saxton (eGS) algorithm

In this paper, we directly extend the eGS technique to a polarization-sensitive modality, and thus we will start with a discussion of the eGS technique. The technique of Gerchberg and Saxton is a phase-retrieval-based wavefront-characterization technique [25,26] wherein the intensity image of a beam is recorded at two planes: one at the focus and one in the far-field. By numerically

Optics EXPRESS

propagating the estimated field between the measurement planes and iteratively enforcing each intensity measurement, the phase profile of the beam can be recovered. This works well in some cases; however, it can fail to retrieve the field even in simple cases such as astigmatic beams. To address this, this technique was extended by Allen and Oxley to include measurements at a series of planes through the focus [24]. This approach, which we refer to as extended Gerchberg–Saxton (eGS), can recover structured beams with scalar polarization [15]. We will use eGS as a step in PeGS to solve for the wavefront of the beam for each orientation of an analyzer.

2.2. Using extended Gerchberg–Saxton for polarimetry

In this section, we describe Polarimetry with extended Gerchberg–Saxton (PeGS), which is our extension of eGS that enables measurement of the polarization spatial distribution of arbitrary beams with high spatial resolution, and is schematized in Fig. 1.

Using Jones calculus, the vector field at one pixel j of an arbitrary beam is written as a two-component vector that contains the amplitude and phase of two orthogonal polarizations:

$$\begin{pmatrix} a_j e^{i\theta_{a_j}} \\ b_j e^{i\theta_{b_j}} \end{pmatrix}. \tag{1}$$

Common in phase retrieval problems, there is an unmeasurable constant phase offset ambiguity. Therefore, when considering a single pixel, the phase of one component can be assumed to be zero; only the amplitude and relative phase of the two components determine that pixel's polarization. Importantly, the full wavefront and polarization spatial distribution of an arbitrary beam can be defined by the complex field for two orthogonal polarizations, and a single, global phase offset between them. The two fields can be measured by recording two eGS datasets, one each for two orthogonal orientations of an analyzer. In other words, a single eGS reconstruction can return the scalar, complex field of the beam for one polarization, with each pixel containing the amplitude of the field at that point, as well as its phase relative to the other pixels within the reconstruction. Unfortunately, the global phase between the two orthogonal polarizations is not possible to determine from these two measurements alone. To solve for the complete light field, we record a third eGS dataset with the analyzer set to mix the two polarizations. Only one relative phase between the two orthogonal fields will match the third measurement. The remainder of Section 2 derives the requisite equations to solve for this global phase offset.

2.3. Solving for global phase offset

If a beam is characterized by eGS after it passes through a linear polarizer oriented horizontally, vertically, and at +45°, we obtain three complex measurements $\tilde{M}$ for each pixel indexed by j:

$$\tilde{M}_{\updownarrow,j} = a_j e^{i\theta_{a_j}} e^{i\theta_{\updownarrow}} \tag{2a}$$

$$\tilde{M}_{\leftrightarrow,j} = b_j e^{i\theta_{b_j}} e^{i\theta_{\leftrightarrow}} \tag{2b}$$

$$\tilde{M}_{\nearrow\!\!\!\swarrow,j} = \frac{1}{\sqrt{2}} \left(a_j e^{i\theta_{a_j}} + b_j e^{i\theta_{b_j}} \right) e^{i\theta_{\nearrow\!\!\!\swarrow}}. \tag{2c}$$

Notably, there is an additional phase component ($\theta_{\updownarrow,\,\leftrightarrow,\nearrow\!\!\!\swarrow}$) for each measurement that represents the constant phase ambiguity that is common between all the pixels in a reconstruction but differs between reconstructions. This is the source of the complication; while each of the reconstructed images shows the phase relationship between the pixels for one polarization, the constant phase ambiguity obfuscates the phase relationship between the three reconstructions.

Our goal is to resolve these phase ambiguities. First, we can set one of them to zero. Here, we select $\theta_{\updownarrow}$, and so $\angle \tilde{M}_{\updownarrow,j} = \theta_{aj}$, where $\angle$ is the phase angle operator. Therefore, in our definition of

Optics EXPRESS

a pixel's polarization state in Eq. (1), the only unknown is θ_{bj}, which we can solve for using the three measurements in Eq. (2). This can done by taking the ratios of Eq. (2a) and (2c):

$$\frac{\tilde{M}_{\swarrow\!\!\!\nearrow,j}}{\tilde{M}_{\updownarrow,j}} = \frac{1}{\sqrt{2}}\left(1 + \frac{b_j e^{i\theta_{b_j}}}{a_j e^{i\theta_{a_j}}}\right) e^{i\theta_{\swarrow\!\!\!\nearrow}}. \tag{3}$$

Then, by taking the magnitude-squared, we eliminate $\theta_{\swarrow\!\!\!\nearrow}$ and obtain the following. Note that $|\tilde{M}_{\updownarrow,j}| = a_j$ and $|\tilde{M}_{\leftrightarrow,j}| = b_j$.

$$\left|\sqrt{2}\frac{\tilde{M}_{\swarrow\!\!\!\nearrow,j}}{\tilde{M}_{\updownarrow,j}}\right|^2 = 1 + \left|\frac{\tilde{M}_{\leftrightarrow,j}}{\tilde{M}_{\updownarrow,j}}\right|^2 + 2\left|\frac{\tilde{M}_{\swarrow\!\!\!\nearrow,j}}{\tilde{M}_{\updownarrow,j}}\right| \cos\left(\theta_{b_j} - \theta_{a_j}\right). \tag{4}$$

From here, Eq. (4) can be used to solve for θ_{bj}:

$$\theta_{b_j} = \angle\tilde{M}_{\leftrightarrow,j} - \theta_{\leftrightarrow} = \angle\tilde{M}_{\updownarrow,j} + \cos^{-1}\left(\frac{\left|\sqrt{2}\frac{\tilde{M}_{\swarrow\!\!\!\nearrow,j}}{\tilde{M}_{\updownarrow,j}}\right|^2 - \left|\frac{\tilde{M}_{\leftrightarrow,j}}{\tilde{M}_{\updownarrow,j}}\right|^2 - 1}{2\left|\frac{\tilde{M}_{\leftrightarrow,j}}{\tilde{M}_{\updownarrow,j}}\right|^2}\right). \tag{5}$$

The solution in Eq. (5) does not completely determine θ_{bj} because inverting the cosine has a sign ambiguity. Fortunately, there is a numeric solution to this problem. To this end, we subtract $\angle\tilde{M}_{\updownarrow}$ from both sides of Eq. (5) and take the absolute value to form the following equation:

$$\left|\angle\tilde{M}_{\leftrightarrow,j} - \theta_{\leftrightarrow} - \angle\tilde{M}_{\updownarrow,j}\right| = \cos^{-1}\left(\frac{\left|\sqrt{2}\frac{\tilde{M}_{\swarrow\!\!\!\nearrow,j}}{\tilde{M}_{\updownarrow,j}}\right|^2 - \left|\frac{\tilde{M}_{\leftrightarrow,j}}{\tilde{M}_{\updownarrow,j}}\right|^2 - 1}{2\left|\frac{\tilde{M}_{\leftrightarrow,j}}{\tilde{M}_{\updownarrow,j}}\right|^2}\right). \tag{6}$$

As shown in Eq. (5), each pixel in the reconstruction has two possible phases of the horizontal field that precedes or follows the vertical field, corresponding to an ambiguity in the handedness of the recovered field at that pixel. Fortunately, Eq. (6) must be satisfied for each pixel in the reconstruction. For most beams, there is only one value of $\theta_{\leftrightarrow}$ that satisfies Eq. (6) for all pixels in the beam; therefore, the task of solving for $\theta_{\leftrightarrow}$ is easily accomplished by performing a linear search for $\theta_{\leftrightarrow}$ that minimizes the difference between the left- and right-hand sides in Eq. (6). While we chose to use +45° orientation of the polarizer in the derivation, it is also possible to do the same for $\tilde{M}_{\nwarrow\!\!\!\searrow,j}$ a measurement taken with −45° orientation; these (and any other results taken at sets of other polarizer angles) can be averaged to mitigate experimental error. It is worth noting that for the −45° orientation, the arccos term in Eq. (5) will pick up a minus sign. Importantly, recording this as an additional dataset can resolve the minor ambiguity noted below.

There is a pathological case that poses an issue for the PeGS technique as described so far. If the beam has uniform polarization everywhere, then its ellipticity can be determined but its handedness cannot. This is the trivial case of the more general ambiguity, in which the phase images of the vertical and horizontal components are the same apart from an overall offset. This corresponds to a constant phase difference between the fields, so the polarization states of the beam all lie on a single half-circumference connecting the vertical and horizontal states on the Poincaré sphere. In this case, the handedness cannot be determined by PeGS as yet described, and two solutions exist that are mirrored across the equator of the Poincaré sphere.

There are two simple modifications to PeGS that each eliminate the ambiguity for non-trivially polarized beams. First, if the amplitude images are different for the two polarizations, then minimizing Eq. (6) at a different plane or across multiple planes will be unique. Second, no beam can suffer this ambiguity for the measurements described and also for measurements

Optics EXPRESS

using a different set of analyzer angles (e.g., ±45° and vertical polarization). Therefore, if the vertical/horizontal basis is unsuitable, then using rotated measurements and minimizing Eq. (6) in the rotated basis will be unique.

We finally note the calibration requirements in PeGS. If the analyzer has a low extinction ratio or depolarizes the light substantially, we anticipate that the solution is likely no longer closed-form and free of ambiguity; however, it may still be possible to find a solution using an iterative method. If the polarizer has a high extinction ratio and low depolarization, the three measurements are characterized by the relative angle of the polarizer between the measurements, as well as their collective rotation relative to known (e.g., horizontal and vertical) axes. The former is easily accomplished with common rotation mounts. As seen in the solution above, the collective rotation plays no role in the solution other than defining the basis that the solution represents. Therefore, if this value is unknown, the solution is the same other than a rotation of unknown magnitude about the poles of the Poincaré sphere. Calibration of PeGS involves a simple process of measuring the absolute orientation of the polarizer to eliminate this uncertainty.

2.4. Summary of the solution

The PeGS algorithm solves for the four unknowns in the Jones calculus representation of an electric field at each pixel, as shown in Eq. (1). This is achieved by collecting three complex wavefront measurements $\tilde{M}$ of the beam. Each measurement is made by using eGS on the beam after it passes through a polarizer at the following angles: two that are orthogonal to each other and one half-way in between. As summarized in Eq. (7), the relative phase between the two orthogonally polarized fields, θ_{bj}, can be obtained using either the $\tilde{M}_{\swarrow\!\!\nearrow}$ or $\tilde{M}_{\nwarrow\!\!\searrow}$ measurement. Importantly, we have assumed a right-handed coordinate system and the camera data oriented with the beam's propagation coming out of the page; mirroring the camera data (often overlooked experimentally) will necessitate inverting the sign of the *min()* term in Eq. (7)c.

$$a_j e^{i\theta_{a_j}} = \tilde{M}_{\updownarrow,j} \tag{7a}$$

$$b_j = |\tilde{M}_{\leftrightarrow,j}| \tag{7b}$$

$$\theta_{b_j} = \angle\tilde{M}_{\leftrightarrow,j} - \min_{\theta_{\leftrightarrow}} \sqrt{\sum \left| \left|\angle\tilde{M}_{\leftrightarrow,j} - \angle\tilde{M}_{\updownarrow,j} - \theta_{\leftrightarrow}\right| - \cos^{-1}\left(\frac{\left|\sqrt{2}\frac{\tilde{M}_{\swarrow\!\!\nearrow,j}}{\tilde{M}_{\updownarrow,j}}\right|^2 - \left|\frac{\tilde{M}_{\leftrightarrow,j}}{\tilde{M}_{\updownarrow,j}}\right|^2 - 1}{2\left|\frac{\tilde{M}_{\leftrightarrow,j}}{\tilde{M}_{\updownarrow,j}}\right|^2} \right) \right|^2} \tag{7c}$$

3. Experimental demonstration of PeGS

To demonstrate the efficacy of PeGS, we test it on three groups of scientifically relevant beams with increasing complexity. First, we illustrate the technique on dual-spot beams that are useful for Fourier transform spectroscopy with high harmonic generation (HHG). Next, we characterize full Poincaré beams that are generated by superposing OAM beams of orthogonal polarizations. These beams fully span the surface of the Poincaré sphere and can be used in a wide variety of applications from machining to imaging due to their unique propagation and scattering resistance characteristics. Finally, we demonstrate PeGS on vector and vector vortex beams that can be used for optical trapping and photoinduced magnetic excitation for their tight-focusing ability.

In each experiment, the same underlying setup was used, with variations introduced for generating the different types of beams, as shown in Fig. 1. A Ti:Sapphire oscillator generates continuous-wave 785 nm light, which is prepared in the desired linear polarization using a half-wave plate. The beam is focused with an $f = 30$ cm lens and then passes through a linear polarizer and onto the camera. The absolute angle of the linear polarizer was measured by using the throughput of the polarizing beamsplitters. Before or in between these PeGS optics, we use other optics to generate characteristic beams that we wish to measure. We record a series of images with the detector moved to known positions through the beam's focus. The detector is an 8-bit CMOS camera (Mightex SME-B050-U with the sensor glass removed to prevent back-reflections), and is moved along the optical axis by a motorized stage (Zaber X-LHM100A). The data range spans roughly 10 cm, sampled at 40 planes evenly spaced through the focus. It is critical that the measurements span the focus; here, the minimum beam diameter is ~165 µm (75 pixels) and the maximum is ~365 µm (166 pixels). At each plane, an exposure time is selected so that the peak intensity is roughly 200 counts. We repeat this data collection for four analyzer orientations (0°, 90°, and ±45°), creating a full eGS dataset for each. Only three are required for the beams studied here, but we recorded the fourth to provide consistency checks of our reconstructions. The images are first cropped to remove regions without signal, then normalized by exposure time to ensure that the intensities are meaningful between frames, and finally processed with the eGS algorithm. The result is a complex field for each polarizer orientation, which can be analyzed by PeGS as discussed in Section 2 to solve for the beam's full polarization state.

3.1. Dual-spot beam

The first group of beams we measured using PeGS were dual-spot beams, which have two lobes of orthogonal polarization at the focal plane. These beams are useful for generating extreme ultraviolet polarization-structured beams using HHG, which can then be used for Fourier transform magneto-optical spectroscopy [28,29]; in these cases, the purity of the polarization states is quite important, as are the positions of the beamlets. Characterizing their relatively simple structure serves as a good pilot demonstration of the PeGS technique. We generated dual-spot beams by focusing a 45° polarized beam through a calcite delay plate (which had been cut at an angle relative to the crystal axis) as shown in Fig. 1(a). Due to the spatial walk-off within the birefringent crystal, the vertical and horizontal components separated by roughly 165 µm at the focus, but overlapped away from the focus.

The reconstruction of the beam at the focal plane is shown in Fig. 2, and can easily be propagated to any other plane, as shown in the insert of Fig. 1(a). Figure 2(a,b) displays the orthogonally polarized components of the beam, where the amplitude is shown as brightness and the phase as hue. Figure 2(c) shows the per-pixel polarization of the beam using the colormap defined on the flattened surface of the Poincaré sphere shown at the bottom-left, and the top-right insert shows the total intensity of the beam. The PeGS technique solves for the polarization state of each pixel, but for visualization purposes, we superimpose polarization ellipses sparsely and over only the higher-intensity regions of the image. A linear phase (corresponding to a non-zero angle between the beam's propagation axis and the camera stage motion) has also been removed from both fields to better visualize the beam's structure. The rest of the reconstructions in this paper (Figs. 2–9) are all shown using the same visualization scheme, also at the focal plane and with the beam's propagation coming out of the page. In Fig. 2, the beamlets can be seen to be both linearly polarized and orthogonal to one another, as expected. Outside the focus, the vertical and horizontal polarizations mix, as shown in the insert of Fig. 1(a).

We then inserted a $\lambda/4$ waveplate after the calcite crystal to give the beamlets circular polarization with opposite handedness, as seen in Fig. 3. As shown, the PeGS method correctly returned the handedness of the two respective beams.

3.2. Full Poincaré beams

OAM beams have a characteristic helix-shaped wavefront that rotates around the propagation axis, and have been used in a wide range of applications from optical communication to super-resolution microscopy [1–3,5,6]. In many cases, the OAM beams are used on their own, but sometimes they

Optics EXPRESS

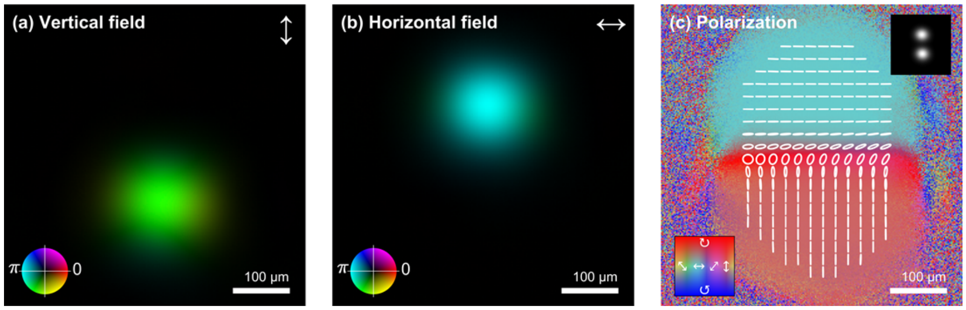

Fig. 2. Linearly polarized dual-spot beam PeGS reconstruction at the focal plane. (a,b) Complex field of the vertically and horizontally polarized components of the beam. Brightness corresponds to field amplitude and hue to phase as shown in the color wheel. (c) High-resolution reconstruction of the beam's polarization. Each pixel's polarization is encoded in the colormap at bottom-left, where each color corresponds to a unique point on the Poincaré sphere [27]. Polarization ellipses are overlaid sparsely for visualization but contain no additional information. All subfigures (a–c) as well as the intensity insert in (c) share the same field of view.

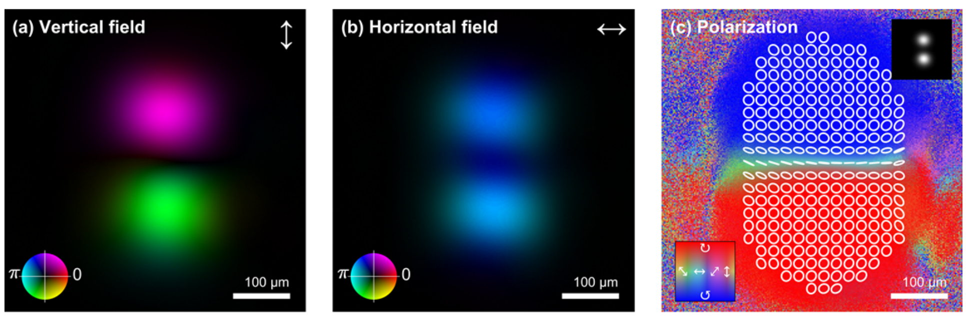

Fig. 3. Circularly polarized dual-spot beam reconstruction. (a,b) Complex field of the vertically and horizontally polarized components of the beam. (c) The polarization spatial distribution of the total beam.

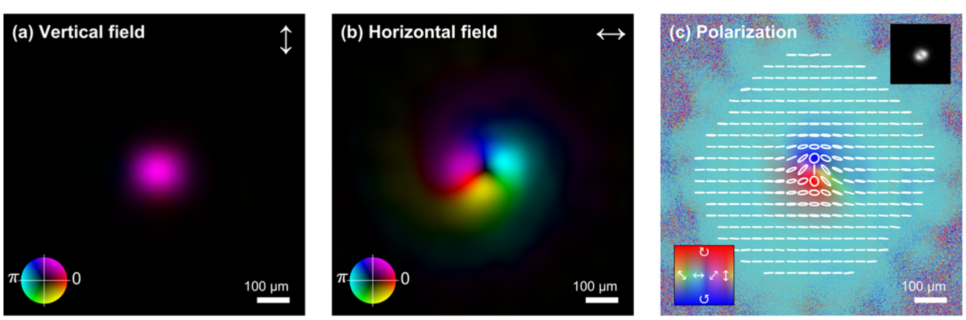

Fig. 4. Full Poincaré beam generated by superimposing a vertically polarized Gaussian beam and a horizontally polarized OAM beam of charge $l = -1$. (a,b) Complex field of the vertically and horizontally polarized components of the beam. (c) The polarization spatial distribution of the total beam.

Optics EXPRESS

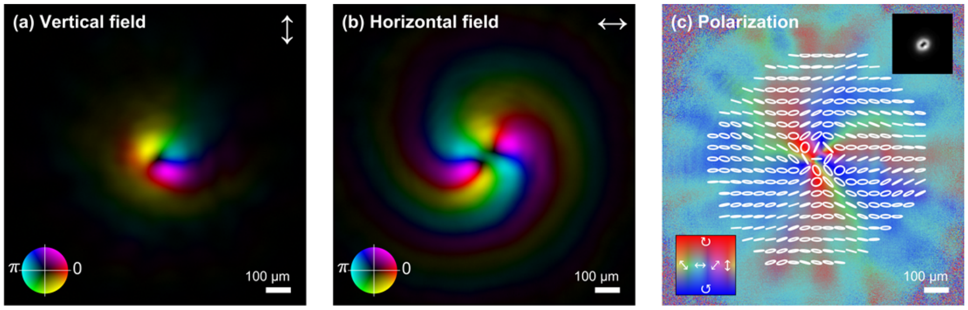

Fig. 5. Full Poincaré beam generated by superimposing a vertically polarized OAM beam of charge $l = +1$ and a vertically polarized OAM beam of charge $l = -2$. (a,b) Complex field of the vertically and horizontally polarized components of the beam. (c) The polarization spatial distribution of the total beam.

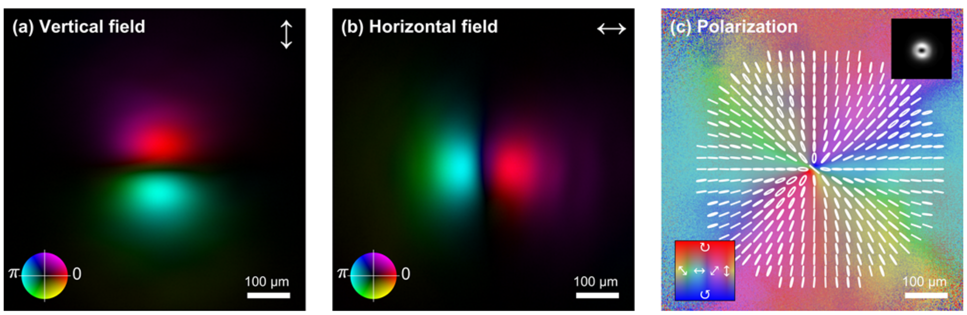

Fig. 6. Vector beam with radial polarization, generated by inputting a horizontally polarized Gaussian beam into an S-waveplate. (a,b) Complex field of the vertically and horizontally polarized components of the beam. (c) The polarization spatial distribution of the total beam.

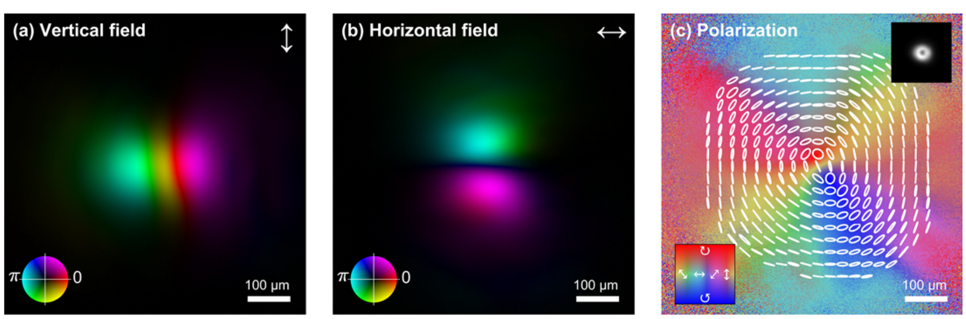

Fig. 7. Vector beam with azimuthal polarization, generated by inputting a vertically polarized Gaussian beam into an S-waveplate. (a,b) Complex field of the vertically and horizontally polarized components of the beam. (c) The polarization spatial distribution of the total beam.

Optics EXPRESS

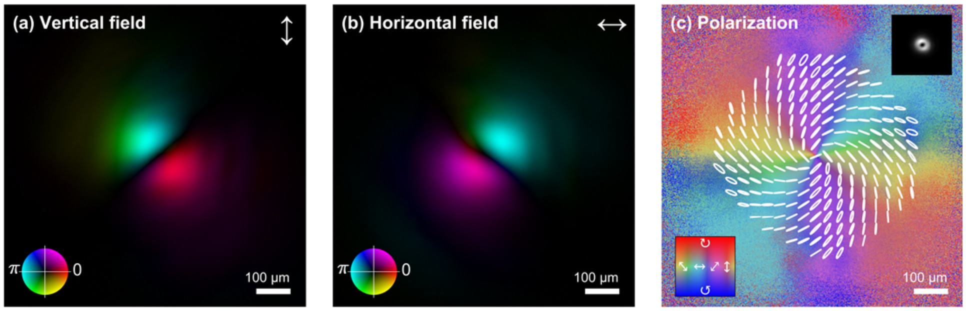

Fig. 8. Vector beam generated by inputting a 45-degree linearly polarized Gaussian beam into an S-waveplate. (a,b) Complex field of the vertically and horizontally polarized components of the beam. (c) The polarization spatial distribution of the total beam.

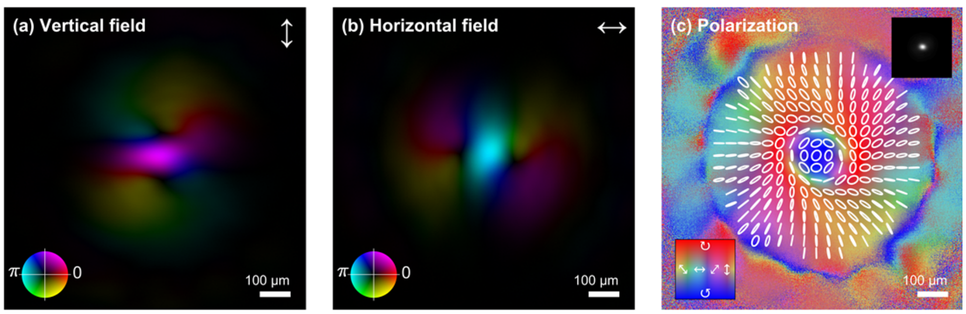

Fig. 9. Vector vortex beam generated by inputting a horizontally polarized OAM beam of charge $l = -1$ into an S-waveplate. (a,b) Complex field of the vertically and horizontally polarized components of the beam. (c) The polarization spatial distribution of the total beam.

can be superposed with each other or other beams to form more complicated beam structures. For example, superpositions of OAM beams have been used with HHG to create short-wavelength beams with exotic structure [30,31]. In these experiments, the alignment and overlap between the two modes is critical; with even a slight misalignment, the structure of the resulting beam can suffer drastically. With a similar setup, full Poincaré beams, which span the entire surface of the Poincaré sphere, can be generated by superimposing orthogonally polarized OAM beams of different charges. These beams can be used in a wide range of applications from laser machining (by forming high quality flattop beams) to communication and imaging (for their scattering resistance in dispersive media) [32–36].

Here, we demonstrate the ability of PeGS to recover with high resolution the overlap, relative tilt, and phase structure of the individual beams when OAM beams of different charge and polarization are superimposed on top of each other. We generated these beams by using variations of a polarizing Mach-Zehnder interferometer, as shown in Fig. 1(b). If there is no optic placed in one of the arms, the beam in that arm remains a Gaussian ($l = 0$) beam, and when spiral phase plates are used, OAM beams with $l = \pm 1$ or ± 2 are generated.

There are multiple combinations of OAM beams that can be superimposed to generate a full Poincaré beam. First, we used an $l = \pm 1$ OAM spiral phase plate (Holo/Or VL-214-795-Y-A) in the horizontally polarized arm of the interferometer and left the vertically polarized arm unaltered as a Gaussian beam. As seen in Fig. 4, we recovered the OAM beam and the Gaussian beam as separate fields and then retrieved the full-field polarization at each pixel. As can be seen in Fig. 4(c), the polarization spatial distribution of the total beam spans a wide range of the polarization colormap, from both handedness of the circular polarization to all the angles of the linear polarization. This is shown in more detail in Section 4.

Next, we placed the $l = \pm 1$ spiral phase plate in the vertically polarized arm and an $l = \pm 2$ spiral phase plate (Holo/Or VL-220-795-Y-A) in the horizontally polarized arm. The result is shown in Fig. 5. There was a slight noncollinearity between the vertical and the horizontal fields, resulting from a slight misalignment of the interferometer. This is visible in Fig. 5(a) as an appearance of asymmetry in the $l = +1$ beam and in the retrieved polarization. That PeGS was able to successfully reveal this misalignment demonstrates its utility in sensitive applications.

3.3. Vector and vector vortex beams (S-waveplate)

Vector and vector vortex beams, which have spatially inhomogeneous polarization distribution and a phase or polarization singularity, are gaining interest for a wide range of applications [37,38]. In particular, radial- and azimuthal-polarization beams are linearly polarized everywhere, but the polarization varies across the beam, with radial or azimuthal isocontours. For example, radial-polarization beams allow very tight focusing, which makes them well-suited for optical trapping and Raman scattering microscopy [39–43]. Azimuthal-polarization beams have a very strong axial magnetic field and near-zero electric field under tight focusing conditions, which makes them useful for photoinduced magnetic excitation [44,45]. These beams are often generated with finely machined optics, such as azimuthally varying retarders (S-waveplates), which are very sensitive to misalignment [46]. Quantitative characterization of this misalignment can be challenging with existing techniques, so we demonstrate PeGS on these beams.

First, a Gaussian beam with a controlled linear polarization was sent into an S-waveplate (Workshop of Photonics RPC-800-15). As expected, when a horizontally polarized beam was used, the S-waveplate produced a beam with radial polarization, shown in Fig. 6. Likewise, a vertically polarized input generated a beam with azimuthal polarization, as shown in Fig. 7. Lastly, a diagonally polarized input produced a mixture of radial and azimuthal polarizations, seen in Fig. 8. We note that, even though the intensity profile of the total beam appears similar between the cases, intensity profiles after the analyzer were distinct and the spatially dependent polarization is exquisitely and uniquely recovered in the final reconstructions. In addition, PeGS also showed slight imperfections in the beams—for example, the lack of separation between the two lobes in Fig. 7(a) suggests a minor misalignment of the experiment.

We also characterized a vector vortex beam that was generated by inputting a horizontally polarized OAM beam of charge $l = -1$ into the S-waveplate. A very similar setup has been used to generate an IR vector vortex driver that was then used to obtain EUV vector vortex beams via HHG [47]. The generated beam has a deceptively simple intensity pattern with a bright central lobe on a pedestal, but PeGS reveals a rich underlying structure: the central lobe has circular polarization, and is surrounded by a ring of azimuthal linear polarization that gradually transitions to a ring of radial polarization.

4. Discussion

As demonstrated in the reconstructions above, PeGS is a powerful technique that can retrieve the full polarization state of very complicated beams, quantitatively and with high resolution (defined by the pixel size of the camera, here 2.2 µm). It requires only a linear polarizer and intensity measurements of the beam through the focus—a relatively simple setup that uses CDI to sidestep the use of a waveplate or careful calibrations.

The reconstructions of a wide range of beams retrieved using PeGS are each consistent with their expected structure. In the polarization spatial distributions plotted in Figs. 2–9(c), the polarizations are very cleanly solved in the central bright parts of the beam with only a small amount of noise, but towards the dimmer outer edges of the beams, the retrieved polarizations become noisier. It is possible to draw an approximate boundary to which PeGS was able to solve

Optics EXPRESS

for the polarization states with high signal-to-noise ratio; we estimate this boundary to be roughly $1/e^6$ of the beam's peak intensity ($1/e^3$ peak amplitude) in these measurements, as displayed by the intensity contour lines plotted in Fig. 10. This is unexpected, considering that we used an 8-bit camera, but can be explained by the fact that each dataset used many camera measurements (40 per polarizer angle).

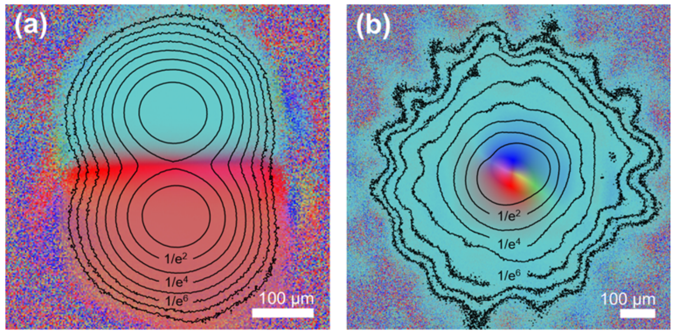

Fig. 10. Polarization spatial distributions with total intensity contours overlaid, spanning from $1/e$ to $1/e^8$ of the peak intensity. We see that the PeGS technique can reliably solve to at least the $1/e^6$ contour for both (a) the linearly polarized dual-spot beam from Fig. 2 and (b) the full Poincaré beam from Fig. 4.

Some of the reconstructions in this paper revealed minor imperfections in the beam, which shows that PeGS can be used to identify experimental misalignments within a physical system. We think that the imperfections seen in our beams are largely explained by simple experimental challenges; for instance, the 785 nm illumination that was used in the experiments had a native slight astigmatism, and this wavelength was at the edge of the bandwidth of the coatings on the polarizing beam splitters.

The simplicity of the PeGS setup is realized through the use of eGS, a computational algorithm; this comes with a minor drawback in that the algorithm can sometimes struggle to converge to the correct solution depending on the signal-to-noise level of the data; the convergence can be monitored by measuring the difference between the amplitudes of the estimated field and the measured data in the eGS algorithm. While there is no simple way to relate the error in the retrieved polarization spatial distribution to the error of the Gerchberg–Saxton algorithm (i.e. difference between the intensity of the collected data and the reconstruction), it is reasonable to assume that they are at least partially correlated. In our reconstructions, in regions with $1/e$ of the peak intensity or above, the mean of the pixel-wise error of the Gerchberg–Saxton algorithms was around 6% (though some of that is due to noise in the data). It should be noted that, despite this level of frame-to-frame error in the Gerchberg–Saxton reconstruction, the precision of the solved-for polarization states can be quite high. For example, in the linearly polarized dual-spot beam in Fig. 10(a), within the $1/e$ intensity contour (where the lobes don't mix and the polarization is mostly constant in each lobe), the standard deviation in the azimuth and the ellipticity angles ranged between 0.4 and 1.9 degrees for both lobes of the beam. In future implementations, the error in the Gerchberg–Saxton algorithm could be further reduced by refining the stage positions within the algorithm to account for slight experimental error. If convergence is poor, it can be improved by using an educated guess for the phase of the field. For example, applying a crude guess with the correct OAM charge sometimes helped OAM beam datasets to converge.

Once the beam's polarization is reconstructed using PeGS, further analysis can be performed on the full vector field. First, the field can be visualized in a polarization basis which is better-suited to describe the behavior of the beam or optical element. For example, the operation of the

S-waveplate is more easily understood in terms of spin angular momentum (SAM, or circular polarization) and OAM of light. As discussed in Gecevičius et al., S-waveplates reverse the handedness of circular polarization, and then add an OAM charge in the new direction of the spin (−1 for right circular, RCP; +1 for left circular, LCP) [48]. This is trivialized in the case of linearly polarized input beams, where both RCP and LCP have equal OAM charge: the S-waveplate subtracts an OAM charge from the RCP beam, and adds one to the LCP beam. This is visualized in Fig. 11, where we cast the radial-polarization beam from Fig. 6 and the vector vortex beam from Fig. 9 into the circular polarization basis. To generate the radial-polarization beam, a horizontally polarized Gaussian beam—in other words, a superposition of identical RCP and LCP beams with $l = 0$—was passed through the S-waveplate. The resultant beam was a superposition of an RCP OAM beam of charge $l = -1$ and an LCP OAM beam of charge $l = +1$. Similarly, to generate the vector vortex beam, the input was equivalent to a superposition of RCP and LCP OAM beams of charge $l = -1$ and the resultant beam was a superposition of an RCP OAM beam of charge $l = -2$ and an LCP OAM beam of charge $l = 0$.

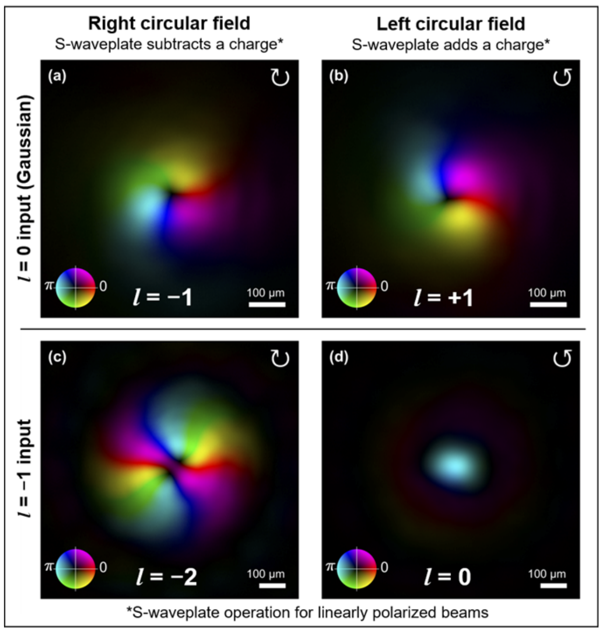

Fig. 11. Beams generated with an S-waveplate shown in the right- and left-handed circular polarization basis (RCP and LCP respectively). For linearly polarized input beams, S-waveplates subtract an OAM charge from the RCP field while adding an OAM charge to the LCP field. (a,b) Complex field of the radial-polarization beam from Fig. 6 cast into the RCP and LCP basis; the beam was generated by sending a horizontally polarized $l = 0$ (Gaussian) beam into the S-waveplate. (c,d) Complex field of the vector vortex beam from Fig. 9 cast into the RCP and LCP basis. The beam was generated by sending a horizontally polarized $l = -1$ OAM beam into the S-waveplate. Note that our coordinate system requires that RCP fields rotate clockwise in time when looking towards the source, and these fields are plotted with the beam's propagation coming out of the page.

Upon comparison of the polarization map in Fig. 9(c) and this representation in the circular polarization basis, we can see how the superposition of the fields yield the observed polarization spatial distribution. The LCP in the central region is attributed to the amplitude minimum of the RCP field and the maximum of the LCP field. Moving outward, we encounter a ring of azimuthal polarization where the RCP and LCP amplitudes are nearly equal, the phase of LCP field is

Optics EXPRESS

roughly constant but the phase of RCP field is rotating through 4π. Progressing further outward, RCP elliptical polarization states arise as the RCP amplitude begins to dominate until once more reaching near-equal amplitudes and radial polarization; the angle of the linear polarizations are rotated by 90 degrees compared to the inner ring of azimuthal polarization, due to the phase of the left circular field having shifted roughly by π.

As another example of analysis that can be performed on full vector fields retrieved by PeGS, the polarization states present in a beam can be plotted over the surface of the Poincaré sphere. This is shown in Fig. 12 for (a) the linear dual-spot beam of Fig. 2 and (b) the full Poincaré beam of Fig. 4. In the figure, each black dot corresponds to a single pixel in the polarization reconstruction and is plotted on the surface of the Poincaré sphere. Pixels that were not reconstructed with enough signal-to-noise ratio were omitted while generating Fig. 12.

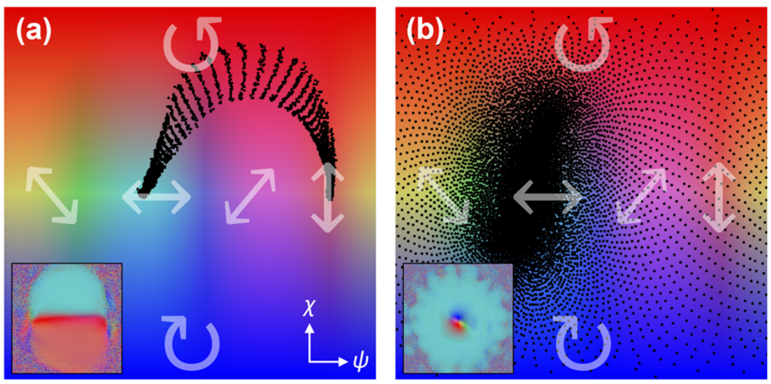

Fig. 12. Polarization states in (a) the linearly polarized dual-spot beam and (b) the superposition of vertically polarized Gaussian beam and the horizontally polarized OAM beam of charge $l = -1$. Each black dot corresponds to a single pixel in the polarization reconstruction and is plotted on the flattened surface of the Poincaré sphere, where the azimuth angle (ψ) has been mapped to the horizontal axis and the ellipticity (χ) has been mapped to the vertical axis. Irregularities in these plots can indicate experiment misalignments. Bottom-left insert shows the polarization plot shown in Fig. 2(c) and 4(c) respectively, with the same colormap shown in the background of the main images.

For the linearly polarized dual-spot beam from Fig. 2, the polarization spatial distribution is mostly split between two linear polarizations, with a transition between the two that approaches LCP. The phase shift between the two beamlets determines the path taken between the two linear polarizations; with a different phase shift, the path could have approached RCP or might have traveled in either direction along the equator of the Poincaré sphere. Black dots appear grouped as a result of the discretized nature of the reconstruction, and each group of dots represents roughly one row of pixels in the reconstruction. The vertical spread corresponds to a different ellipticity at each y-coordinate in the low-intensity region between the two spots, and is caused by a slight astigmatism in the beam before it entered the calcite plate.

For the superposition of the vertically polarized Gaussian beam and the horizontally polarized $l = -1$ OAM beam from Fig. 4, the black dots cover the entire surface of the Poincaré sphere, showing that this beam is indeed a full Poincaré beam. The high concentration of dots at the horizontal linear polarization is due to the fact that the horizontally polarized OAM beam was larger than the Gaussian beam, so the pixels at the outer edge of their superposition were mostly horizontally polarized.

5. Conclusion

We have shown that combining the extended Gerchberg–Saxton phase retrieval technique with a polarizer enables a novel wavefront-sensing polarimeter that achieves high-resolution mapping of the polarization spatial distribution of arbitrary beams with minimal optics or alignment [15]. New methods for computational phase retrieval and polarimetry are a topic of much interest as researchers develop and use novel structured light beams for imaging and metrology, or for characterizing and diagnosing optical systems. The technique does not need multiple, well-calibrated optics, and is applicable to the extreme UV and soft X-ray regions of the spectrum, where in many cases, optics are either unavailable, imperfect or lossy.

Funding. STROBE: A National Science Foundation Science & Technology Center (DMR 1548924).

Acknowledgments. We thank J. Curtis Beimborn II and Michaël Hemmer for their help in implementing the experimental setup.

Disclosures. H.K.: KMLabs Inc. (I, E). M.M.: KMLabs Inc. (I). Other authors declare no conflicts of interest.

Data availability. Data underlying the results presented in this paper are not publicly available at this time but may be obtained from the authors upon reasonable request.

References

1. B. Wang, M. Tanksalvala, Z. Zhang, Y. Esashi, N. W. Jenkins, M. M. Murnane, H. C. Kapteyn, and C.-T. Liao, "Coherent Fourier scatterometry using orbital angular momentum beams for defect detection," Opt. Express **29**(3), 3342–3358 (2021).
2. G. Gibson, J. Courtial, M. J. Padgett, M. Vasnetsov, V. Pas'ko, S. M. Barnett, and S. Franke-Arnold, "Free-space information transfer using light beams carrying orbital angular momentum," Opt. Express **12**(22), 5448–5456 (2004).
3. J. Wang, J. Y. Yang, I. M. Fazal, N. Ahmed, Y. Yan, H. Huang, Y. Ren, Y. Yue, S. Dolinar, M. Tur, and A. E. Willner, "Terabit free-space data transmission employing orbital angular momentum multiplexing," Nat. Photonics **6**(7), 488–496 (2012).
4. I. Saraeva, S. I. Kudryashov, P. Danilov, N. Busleev, E. R. Tolordava, A. A. Rudenko, D. Zayarny, A. Ionin, and Y. M. Romanova, "Polarization-sensitive surface-enhanced in situ photoluminescence spectroscopy of s. Aureus bacteria on gold nanospikes," Sensors **20**(9), 2466 (2020).
5. G. Vicidomini, P. Bianchini, and A. Diaspro, "STED super-resolved microscopy," Nat. Methods **15**(3), 173–182 (2018).
6. Y. Shen, X. Wang, Z. Xie, C. Min, X. Fu, Q. Liu, M. Gong, and X. Yuan, "Optical vortices 30 years on: OAM manipulation from topological charge to multiple singularities," Light: Science and Applications **8**(90), 1–29 (2019).
7. C. Rosales-Guzmán, B. Ndagano, and A. Forbes, "A review of complex vector light fields and their applications," J. Opt. **20**, 123001 (2018).
8. D. M. Wulstein and R. McGorty, "Point-spread function engineering enhances digital Fourier microscopy," Opt. Lett. **42**(22), 4603–4606 (2017).
9. E. J. Botcherby, R. Juškaitis, M. J. Booth, and T. Wilson, "An optical technique for remote focusing in microscopy," Opt. Commun. **281**(4), 880–887 (2008).
10. M. Sato, T. Higuchi, N. Kanda, K. Konishi, K. Yoshioka, T. Suzuki, K. Misawa, and M. Kuwata-Gonokami, "Terahertz polarization pulse shaping with arbitrary field control," Nat. Photonics **7**(9), 724–731 (2013).
11. D. D. Hickstein, F. J. Dollar, P. Grychtol, J. L. Ellis, R. Knut, C. Hernández-García, D. Zusin, C. Gentry, J. M. Shaw, T. Fan, K. M. Dorney, A. Becker, A. Jaroń-Becker, H. C. Kapteyn, M. M. Murnane, and C. G. Durfee, "Non-collinear generation of angularly isolated circularly polarized high harmonics," Nat. Photonics **9**(11), 743–750 (2015).
12. L. Loetgering, M. Baluktsian, K. Keskinbora, R. Horstmeyer, T. Wilhein, G. Schütz, K. S. E. Eikema, and S. Witte, "Generation and characterization of focused helical x-ray beams," Sci. Adv. **6**(7), eaax8836 (2020).
13. T. Fan, P. Grychtol, R. Knut, C. Hernández-García, D. D. Hickstein, D. Zusin, C. Gentry, F. J. Dollar, C. A. Mancuso, C. W. Hogle, O. Kfir, D. Legut, K. Carva, J. L. Ellis, K. M. Dorney, C. Chen, O. G. Shpyrko, E. E. Fullerton, O. Cohen, P. M. Oppeneer, D. B. Milošević, A. Becker, A. A. Jaroń-Becker, T. Popmintchev, M. M. Murnane, and H. C. Kapteyn, "Bright circularly polarized soft X-ray high harmonics for X-ray magnetic circular dichroism," Proc. Natl. Acad. Sci. **112**(46), 14206–14211 (2015).
14. C. Chen, Z. Tao, C. Hernández-García, P. Matyba, A. Carr, R. Knut, O. Kfir, D. Zusin, C. Gentry, P. Grychtol, O. Cohen, L. Plaja, A. Becker, A. Jaron-Becker, H. Kapteyn, and M. Murnane, "Tomographic reconstruction of circularly polarized high-harmonic fields: 3D attosecond metrology," Sci. Adv. **2**(2), e1501333 (2016).
15. L. Rego, K. M. Dorney, N. J. Brooks, Q. L. Nguyen, C. T. Liao, J. S. Román, D. E. Couch, A. Liu, E. Pisanty, M. Lewenstein, L. Plaja, H. C. Kapteyn, M. M. Murnane, and C. Hernández-García, "Generation of extreme-ultraviolet beams with time-varying orbital angular momentum," Science **364**(6447), eaaw9486 (2019).
16. N. A. Rubin, A. Zaidi, M. Juhl, R. P. Li, J. P. B. Mueller, R. C. Devlin, K. Leósson, and F. Capasso, "Polarization state generation and measurement with a single metasurface," Opt. Express **26**(17), 21455–21478 (2018).

17. M. A. G. Abushagur and A. M. El-Saba, "Lenslet-array-based Stokes vector imagery," Proc. SPIE **5432**, 127–133 (2004).
18. B. Zhao, X.-B. Hu, V. Rodríguez-Fajardo, Z.-H. Zhu, W. Gao, A. Forbes, and C. Rosales-Guzmán, "Real-time Stokes polarimetry using a digital micromirror device," Opt. Express **27**(21), 31087–31093 (2019).
19. M. V. Putintseva, E. T. Aksenov, C. C. Korikov, and E. N. Velichko, "Non-invasive research of biological objects by the method of laser polarimetry," J. Phys.: Conf. Ser. **1124**(3), 031021 (2018).
20. Z. Yang, Z. Wang, Y. Wang, X. Feng, M. Zhao, Z. Wan, L. Zhu, J. Liu, Y. Huang, J. Xia, and M. Wegener, "Generalized Hartmann-Shack array of dielectric metalens sub-arrays for polarimetric beam profiling," Nat. Commun. **9**(4607), 1–7 (2018).
21. C. He, H. He, J. Chang, B. Chen, H. Ma, and M. J. Booth, "Polarisation optics for biomedical and clinical applications: a review," Light: Sci. Appl. **10**(194), 1–20 (2021).
22. J. M. Rodenburg and H. M. L. Faulkner, "A phase retrieval algorithm for shifting illumination," Appl. Phys. Lett. **85**(20), 4795–4797 (2004).
23. Y. Esashi, C.-T. Liao, B. Wang, N. Brooks, K. M. Dorney, C. Hernández-García, H. Kapteyn, D. Adams, and M. Murnane, "Ptychographic amplitude and phase reconstruction of bichromatic vortex beams," Opt. Express **26**(26), 34007–34915 (2018).
24. L. J. Allen and M. P. Oxley, "Phase retrieval from series of images obtained by defocus variation," Opt. Commun. **199**(1-4), 65–75 (2001).
25. R. W. Gerchberg and W. O. Saxton, "A practical algorithm for the determination of phase from image and diffraction plane pictures," Optik (Stuttg) **35**, 237–246 (1972).
26. D. L. Misell, "A method for the solution of the phase problem in electron microscopy," J. Phys. D: Appl. Phys. **6**(1), L6–L9 (1973).
27. J. Wang, F. Castellucci, and S. Franke-Arnold, "Vectorial light–matter interaction: Exploring spatially structured complex light fields," AVS Quantum Science **2**(3), 031702 (2020).
28. A. de Beurs, X. Liu, G. S. Matthijs Jansen, K. S. E. Eikema, and S. Witte, "Rotational Diffractive Shear Interferometry for extreme ultraviolet Imaging," in *Imaging and Applied Optics 2019 (COSI, IS, MATH, PcAOP)* (OSA, 2019), p. CM1A.3.
29. J. L. Ellis, K. M. Dorney, D. D. Hickstein, N. J. Brooks, C. Gentry, C. Hernández-García, D. Zusin, J. M. Shaw, Q. L. Nguyen, C. A. Mancuso, G. S. Matthijs Jansen, S. Witte, H. C. Kapteyn, and M. M. Murnane, "High harmonics with spatially varying ellipticity," Optica **5**(4), 479–485 (2018).
30. K. M. Dorney, L. Rego, N. J. Brooks, J. San Román, C. T. Liao, J. L. Ellis, D. Zusin, C. Gentry, Q. L. Nguyen, J. M. Shaw, A. Picón, L. Plaja, H. C. Kapteyn, M. M. Murnane, and C. Hernández-García, "Controlling the polarization and vortex charge of attosecond high-harmonic beams via simultaneous spin–orbit momentum conservation," Nat. Photonics **13**(2), 123–130 (2019).
31. L. Rego, N. J. Brooks, Q. L. D. Nguyen, J. S. Román, I. Binnie, L. Plaja, H. C. Kapteyn, M. M. Murnane, and C. Hernández-García, "Necklace-structured high-harmonic generation for low-divergence, soft x-ray harmonic combs with tunable line spacing," Sci. Adv. **8**(5), eabj7380 (2022).
32. A. M. Beckley, T. G. Brown, and M. A. Alonso, "Full Poincaré beams," Opt. Express **18**(10), 10777–10785 (2010).
33. W. Han, W. Cheng, and Q. Zhan, "Flattop focusing with full Poincaré beams under low numerical aperture illumination," Opt. Lett. **36**(9), 1605–1607 (2011).
34. H. Wang, G. Rui, and Q. Zhan, "Dynamic propagation of optical vortices embedded in full Poincaré beams with rotationally polarization symmetry," Opt. Commun. **351**, 15–25 (2015).
35. I. Gianani, A. Suprano, T. Giordani, N. Spagnolo, F. Sciarrino, D. Gorpas, V. Ntziachristos, K. Pinker, N. Biton, J. Kupferman, and S. Arnon, "Transmission of vector vortex beams in dispersive media," Adv. Photonics **2**(03), 1–8 (2020).
36. A. de las Heras, A. K. Pandey, J. San Román, J. Serrano, E. Baynard, G. Dovillaire, M. Pittman, C. G. Durfee, L. Plaja, S. Kazamias, O. Guilbaud, and C. Hernández-García, "Extreme-ultraviolet vector-vortex beams from high harmonic generation," Optica **9**(1), 71–79 (2022).
37. C. Hernández-García, A. Turpin, J. San Román, A. Picón, R. Drevinskas, A. Cerkauskaite, P. G. Kazansky, C. G. Durfee, and Í. J. Sola, "Extreme ultraviolet vector beams driven by infrared lasers," Optica **4**(5), 520–526 (2017).
38. A. L. Sokolov and V. V. Murashkin, "Retroreflective spatial-polarization interferometer," Appl. Opt. **59**(32), 9912–9923 (2020).
39. Q. Zhan, "Trapping metallic Rayleigh particles with radial polarization," Opt. Express **12**(15), 3377–3382 (2004).
40. R. Dorn, S. Quabis, and G. Leuchs, "Sharper Focus for a Radially Polarized Light Beam," Phys. Rev. Lett. **91**(23), 233901 (2003).
41. G. M. Lerman and U. Levy, "Radial polarization interferometer," Opt. Express **17**(25), 23234–23246 (2009).
42. F. Lu, W. Zheng, and Z. Huang, "Coherent anti-Stokes Raman scattering microscopy using tightly focused radially polarized light," Opt. Lett. **34**(12), 1870–1872 (2009).
43. A. Yang, L. Du, X. Dou, F. Meng, C. Zhang, C. Min, J. Lin, and X. Yuan, "Sensitive Gap-Enhanced Raman Spectroscopy with a Perfect Radially Polarized Beam," Plasmonics **13**(3), 991–996 (2018).
44. C. Guclu, M. Veysi, and F. Capolino, "Photoinduced Magnetic Nanoprobe Excited by an Azimuthally Polarized Vector Beam," ACS Photonics **3**(11), 2049–2058 (2016).

Optics EXPRESS

45. J. Zeng, F. Huang, C. Guclu, M. Veysi, M. Albooyeh, H. K. Wickramasinghe, and F. Capolino, "Sharply Focused Azimuthally Polarized Beams with Magnetic Dominance: Near-Field Characterization at Nanoscale by Photoinduced Force Microscopy," ACS Photonics **5**(2), 390–397 (2018).
46. M. Beresna, M. Gecevičius, P. G. Kazansky, and T. Gertus, "Radially polarized optical vortex converter created by femtosecond laser nanostructuring of glass," Appl. Phys. Lett. **98**(20), 201101 (2011).
47. A. Caretta, S. Laterza, V. Bonanni, R. Sergo, C. Dri, G. Cautero, F. Galassi, M. Zamolo, A. Simoncig, M. Zangrando, A. Gessini, S. D. Zilio, R. Flammini, P. Moras, A. Demidovich, M. Danailov, F. Parmigiani, and M. Malvestuto, "A novel free-electron laser single-pulse Wollaston polarimeter for magneto-dynamical studies," Struct. Dyn. **8**(3), 034304 (2021).
48. M. Gecevičius, R. Drevinskas, M. Beresna, and P. G. Kazansky, "Single beam optical vortex tweezers with tunable orbital angular momentum," Appl. Phys. Lett. **104**(23), 231110 (2014).